PNAS RESEARCH ARTICLE | PHYSIOLOGY

Functional determination of calcium-binding sites required for the activation of inositol 1,4,5-trisphosphate receptors

Vikas Arige[a,1], Lara E. Terry[a,1], Larry E. Wagner II[a,1], Sundeep Malik[a], Mariah R. Baker[b], Guizhen Fan[b], Suresh K. Joseph[c], Irina I. Serysheva[b,2], and David I. Yule[a,2]

Edited by Andrew Marks, Columbia University College of Physicians & Surgeons, New York, NY; received June 1, 2022; accepted August 23, 2022

Inositol 1,4,5-trisphosphate receptors (IP_3Rs) initiate a diverse array of physiological responses by carefully orchestrating intracellular calcium (Ca^{2+}) signals in response to various external cues. Notably, IP_3R channel activity is determined by several obligatory factors, including IP_3, Ca^{2+}, and ATP. The critical basic amino acid residues in the N-terminal IP_3-binding core (IBC) region that facilitate IP_3 binding are well characterized. In contrast, the residues conferring regulation by Ca^{2+} have yet to be ascertained. Using comparative structural analysis of Ca^{2+}-binding sites identified in two main families of intracellular Ca^{2+}-release channels, ryanodine receptors (RyRs) and IP_3Rs, we identified putative acidic residues coordinating Ca^{2+} in the cytosolic calcium sensor region in IP_3Rs. We determined the consequences of substituting putative Ca^{2+} binding, acidic residues in IP_3R family members. We show that the agonist-induced Ca^{2+} release, single-channel open probability (P_0), and Ca^{2+} sensitivities are markedly altered when the negative charge on the conserved acidic side chain residues is neutralized. Remarkably, neutralizing the negatively charged side chain on two of the residues individually in the putative Ca^{2+}-binding pocket shifted the Ca^{2+} required to activate IP_3R to higher concentrations, indicating that these residues likely are a component of the Ca^{2+} activation site in IP_3R. Taken together, our findings indicate that Ca^{2+} binding to a well-conserved activation site is a common underlying mechanism resulting in increased channel activity shared by IP_3Rs and RyRs.

inositol 1,4,5 triphosphate receptor | calcium signaling | ion channel regulation

An increase in the intracellular calcium concentration ($[Ca^{2+}]_i$) is essential for innumerable fundamental biological processes. Following stimulation, the concerted action of a diverse array of proteins, collectively termed the Ca^{2+} signaling "toolkit," functions to increase and sequester Ca^{2+} to precisely define the spatiotemporal characteristics of Ca^{2+} signals necessary to control diverse physiological endpoints with specificity and fidelity (1, 2). As a function of exquisite regulation of their activity by a multitude of diverse modulatory inputs, the inositol 1,4,5-trisphosphate receptor family (IP_3R) of Ca^{2+} release channels are a central component of this cellular machinery. In vertebrates, there are three genes that code for IP_3R, *ITPR1–3*, which result in three distinct IP_3R subtypes: IP_3R type 1 (IP_3R1), IP_3R type 2 (IP_3R2), and IP_3R type 3 (IP_3R3), which share approximately 60 to 70% amino acid sequence identity (3–7). IP_3Rs are ubiquitously expressed and predominantly localized to the endoplasmic reticulum (ER) membrane, where functionally they are assembled as either homo- or heterotetramers. While binding of IP_3, generated as a result of the activation of phospholipase C is necessary to gate the channel, it is also clear that the binding of Ca^{2+} itself is obligatory to activate the receptor (8). Thus, IP_3 and Ca^{2+} are considered coagonists of IP_3R (9).

Early work using truncated IP_3R1 established that the N-terminal 788 amino acid residues were required to bind IP_3. Subsequently, mutagenesis approaches established the minimal IP_3-binding core (IBC, residues 224 to 557) and identified the positively charged residues required for coordinating the phosphate moieties in IP_3 (10). More recent X-ray crystallography of the isolated IBC domains (11, 12) and single-particle cryoelectron microscopy (cryo-EM) studies (13–16) have revealed the conserved three-dimensional architecture of the ligand-binding domains (LBDs) that includes β-trefoil domains (β-TF1) (residues 1 to 225) and βTF2 (residues 226 to 435), and a helical armadillo repeat, ARM1 domain (residues 436 to 665), providing structural determinants for the coordination of IP_3 and adenophostin A, a structural mimetic of IP_3, in the IP_3-binding pocket. These studies showed that ligand binding is accompanied by conformational changes in the LBDs (11, 12, 14, 15) and also involves global conformational changes in the cytoplasmic scaffold connected to the channel pore (14, 15). Critically, the functional relevance of these residues has also been confirmed by mutagenesis (17). Indeed, one of the residues (R269) important for IP_3 binding is the locus

Significance

The inositol 1,4,5-trisphosphate receptor (IP_3R) Ca^{2+} release channel is a key component of the Ca^{2+} signaling cellular machinery. Regulation of IP_3R activity is fundamental for defining the spatiotemporal characteristics of Ca^{2+} signals important for the appropriate activation of effectors. The most important regulator of IP_3R activity is an increase in $[Ca^{2+}]$ itself, which initially activates and then, at higher concentrations, inhibits channel activity. While the residues in IP_3R important for IP_3 binding are established, the motifs that coordinate Ca^{2+} have not been functionally determined. Based on predictions from recently published cryo-EM structures of IP_3Rs, we used imaging techniques and electrophysiology to experimentally define the identity of the evolutionarily well-conserved residues in IP_3Rs essential for Ca^{2+} binding and channel activation.

Author contributions: D.I.Y., S.K.J., and I.I.S. conceived of the project; S.K.J., I.I.S., and D.I.Y. designed research; V.A., L.E.T., L.E.W., S.M., M.R.B., and G.F. performed research; V.A. and L.E.T. performed mutagenesis, created stable cell lines and performed imaging experiments; L.E.W. performed single-channel measurements; S.M. performed immunocytochemistry experiments; V.A., L.E.T., L.E.W., and M.R.B. analyzed data; V.A., M.R.B., G.F., I.I.S., and D.I.Y. wrote the paper; and all authors approved of the submission.

The authors declare no competing interest.

This article is a PNAS Direct Submission.

See online for related content such as Commentaries.

[1] V.A., L.E.T., and L.E.W. contributed equally to this work.

[2] To whom correspondence may be addressed. Email: Irina.I.Serysheva@uth.tmc.edu or David_Yule@urmc.rochester.edu.

This article contains supporting information online at http://www.pnas.org/lookup/suppl/doi:10.1073/pnas.2209267119/-/DCSupplemental.

of a point mutation (R269W) that results in spino-cerebellar ataxia in patients as a result of a poorly functional IP_3R1 (18). Furthermore, the mutagenesis of these residues, in increasing numbers of IP_3R monomers within a concatenated tetramer, has led to the demonstration that IP_3 binding to all four subunits in an IP_3R tetramer is an absolute prerequisite for channel opening (19).

Extensive functional characterization at the level of Ca^{2+} release and at the single-channel level have demonstrated that Ca^{2+} modulates IP_3R channel opening in a complex manner (8, 20–25). In the presence of IP_3, low concentrations of Ca^{2+} (<300 nM) facilitate channel opening; however, at higher concentrations, Ca^{2+} promotes channel closure to result in a bell-shaped regulation of IP_3R activity (8). These data are consistent with Ca^{2+} interacting at two distinct sites, one that results in activation and a further site that attenuates activity (26). Models of this regulation have postulated that IP_3 binding modulates the affinity of the Ca^{2+}-binding sites for Ca^{2+} to favor increased or decreased IP_3R channel activity (24, 27–30). This control of IP_3R activity by the interplay between coagonists is widely considered to mechanistically underlie the hierarchy of Ca^{2+} signaling events observed in cells, including localized Ca^{2+} blips, Ca^{2+} puffs, propagating Ca^{2+} waves, and Ca^{2+} oscillations (21, 31–33).

While the determinants of IP_3 binding are firmly established (10), elucidating the motifs that coordinate Ca^{2+} in IP_3R have proved elusive and have yet to be functionally determined (34). Notably, using gel overlay assays, several linear fragments of IP_3R across various domains were shown to bind $^{45}Ca^{2+}$ (35, 36). Nevertheless, point mutations at conserved acidic amino acids in regions identified in the IBC were without any effect on Ca^{2+}-dependent activation of IP_3R, ruling out the possibility of Ca^{2+}-binding site(s) in this domain (37). A further series of studies proposed glutamate (E) 2101 (Fig. 1*B*) as a key residue in IP_3R for activation by Ca^{2+}. Mutating this residue diminished Ca^{2+} sensitivity for activation of IP_3R1 several-fold, but it also altered the IP_3R sensitivity to inhibition by Ca^{2+} (38, 39). Nevertheless, there is little structural evidence supporting direct binding of this residue to Ca^{2+}, indicating that this site perhaps has an allosteric role in stabilizing a confirmation favoring Ca^{2+} binding to bona fide Ca^{2+}-binding site(s) (21, 27).

Perhaps the best clues to potential Ca^{2+}-binding sites in IP_3R come from structural studies of the ryanodine receptor (RyR) (38–40). IP_3Rs share structural and functional features with RyRs; both are intracellular Ca^{2+} release channels with tetrameric architecture and are regulated in a biphasic manner by Ca^{2+} (8). The cryo-EM structure of RyR determined in the presence and absence of its activating ligands (Ca^{2+}/adenosine triphosphate [ATP]/caffeine) revealed several regions that coordinate Ca^{2+} ions in RyRs. These include paired EF-hand domains in the central region of RyR and a pocket of negatively charged residues in the core solenoid and C-terminal domain (40). While mutation of the EF hands did not alter Ca^{2+} activation of RyR2, mutation of the putative binding pocket in RyR1/2 altered Ca^{2+}-dependent activation of RyRs (41, 42). Of note, an analogous Ca^{2+}-binding site is present in the juxta membrane domain of IP_3R between the third armadillo repeat (ARM3) and linker (LNK) domains and is conserved in IP_3Rs across species and through IP_3R subtypes (43). Two cryo-EM studies of human IP_3R3 in the presence of IP_3 and Ca^{2+} have suggested two Ca^{2+}-binding sites, including a site within the putative Ca^{2+} sensor regions located at the interface between the ARM3 (residues 1,587 to 2,119) and LNK (residues 2,538 to 2,608) domains (15, 44). The first structure (15, 44) was solved in supra-physiological [Ca^{2+}], but the limited resolution of the reconstruction precludes the identification of any structural determinants within the Ca^{2+}-binding pockets. Moreover, the channel pore was not engaged under the aforementioned conditions; therefore, it is unclear whether either site relates to stimulation or inhibition of the channel. A second recent human IP_3R3 (hIP_3R3) structure solved at 3.6 Å resolution under more physiological [Ca^{2+}] reported a Ca^{2+} density in the putative Ca^{2+} sensor region in two structures extracted from the same cryo-EM dataset (44). In one of their reported structures, the ion conduction pore was dilated to allow the passage of Ca^{2+}. However, the functional role of this Ca^{2+} binding site remains to be elucidated.

In this study, based on our single-particle cryo-EM structure of IP_3R1 determined at ∼3.26 Å resolution (45), in which a clear interaction between Ca^{2+} and the putative Ca^{2+} sensor region is documented, we performed a series of experiments to examine the consequences of substituting putative Ca^{2+} binding-conserved residues in IP_3R subtypes. We generated stable cell lines expressing wild-type (WT) IP_3Rs and compared agonist-evoked Ca^{2+} release, Ca^{2+} puffs, and single-channel properties with their counterparts harboring substitutions at putative Ca^{2+} coordinating sites. Neutralizing the negative charge on side chain residues at these conserved Ca^{2+} coordinating residues decimated both Ca^{2+} release and Ca^{2+} puff activity evoked by IP_3-generating agonists. Remarkably, substitution with a smaller but similarly charged residue markedly diminished agonist-induced Ca^{2+} release and Ca^{2+} puffs compared to their WT counterparts. Of note, comparison of single-channel properties revealed that the Ca^{2+} sensitivity was dramatically right shifted by charge neutralization, indicating that this site is likely the Ca^{2+} activation site. In contrast, retaining charge on the side chain residue had little effect on Ca^{2+} sensitivity; however, open probability of channel was significantly diminished. Overall, our investigations demonstrate a critical role for the negative charge on side chains of conserved Ca^{2+} coordinating residues in IP_3Rs for electrostatic interactions with Ca^{2+} to facilitate channel opening and subsequent activation of agonist-induced Ca^{2+} release.

Results

Identification of Putative Ca^{2+} Coordinating Residues in IP_3Rs. Our high-resolution cryo-EM structures of rat IP_3R1 (rIP_3R1) in physiologically relevant Ca^{2+}-bound states in the presence or absence of IP_3 and ATP clearly identifies Ca^{2+} bound in the putative Ca^{2+} sensor site formed by E1978, E2042 (in the ARM3 domain, chartreuse), and T2657 residue (in the LNK domain, orange), corresponding to E1938, E2002, and T2614 in the human sequence (Fig. 1*A*), respectively (45). A comparative structural alignment strongly indicates that a putative Ca^{2+} sensor site in rIP_3R1 is analogous to the Ca^{2+}-binding pockets in IP_3R3 (tan, PDB ID: 6DR2) and RyR1 (gray, PDB ID: 5T15) (Fig. 1*B*). Moreover, the three aforementioned residues constituting the putative Ca^{2+} sensor site in human IP_3R1 (hIP_3R1) are well conserved across all hIP_3R (15) and RyR subtypes (40, 41, 43) (Fig. 1*C*). Strikingly, these residues are also highly conserved in the evolution of IP_3R and RyR proteins across various organisms (*SI Appendix*, Fig. S1*A*). In contrast, the putative Ca^{2+}-binding pocket located between the α-helical domain (HD) and the ARM2 in hIP_3R3 (15) is not conserved between RyRs and IP_3Rs (*SI Appendix*, Fig. S1*B*). In addition,

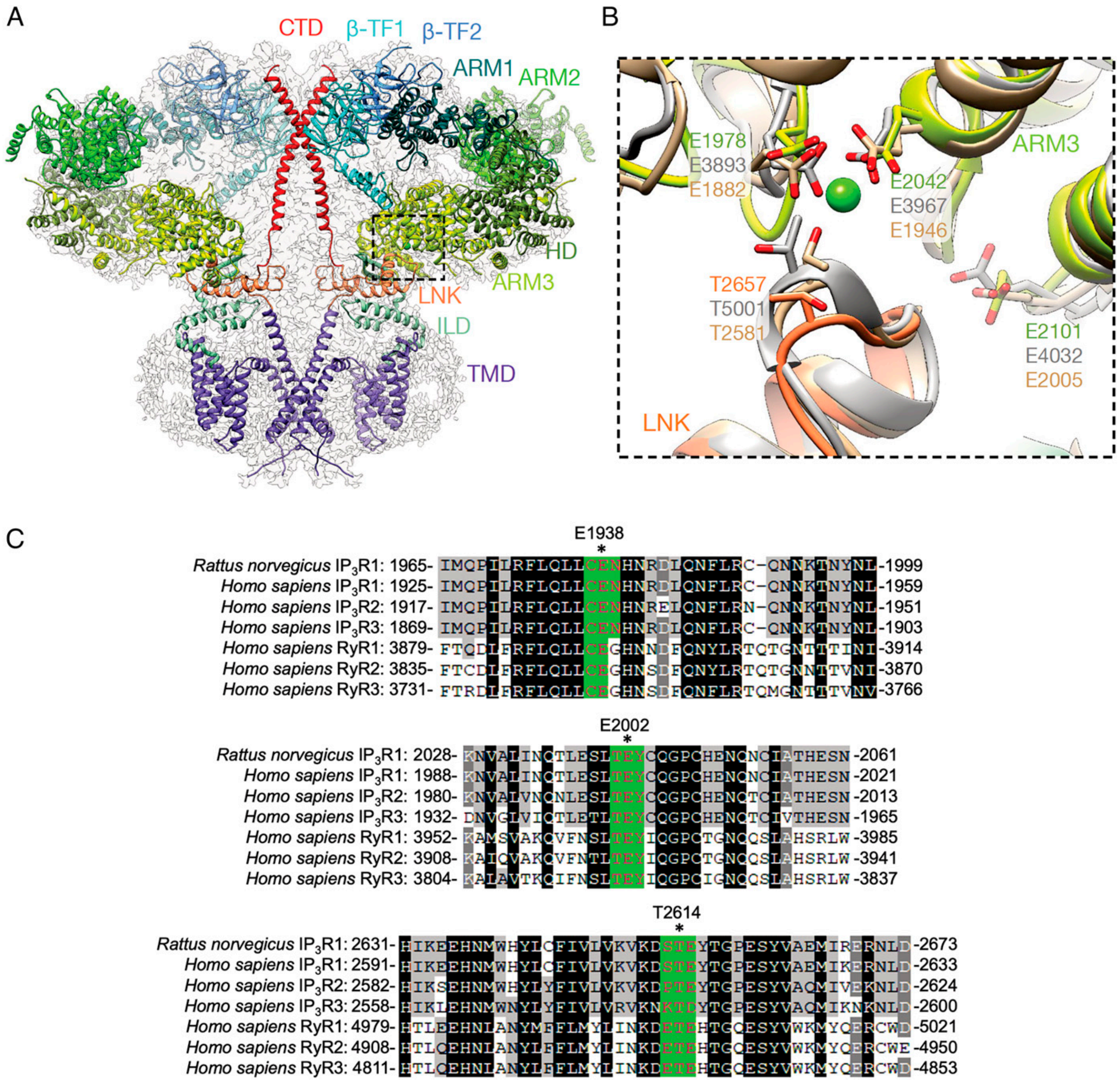

Fig. 1. Structural and sequence conservation of the Ca^{2+}-binding site across IP_3R and RyR families of Ca^{2+} release channels. (*A*) Two opposite subunits in the rat IP_3R1 are color-coded by domains and overlaid with cryo-EM density. (*B*) Structural alignment of IP_3R1 Ca^{2+}-binding sensor domain (indicated with dashed line in (A); PDB ID: 8EAQ; EMDB: EMD-27982 in (45) with IP_3R3 (tan, PDB ID: 6UQK) and RyR1 (gray, PDB ID: 5T15) Ca^{2+}-binding pockets with identical residues labeled. The equivalent human residues in IP_3R1 that form the Ca^{2+} binding pocket are hE1938/rE1978, hE2002/rE2042, hT2614/rT2657, and hE2109/rE2101. (*C*) Sequence alignment for the Ca^{2+}-sensor region across all three IP_3R and RyR subtypes. The conserved E1938, E2002, and T2614 residues in IP_3R1 are highlighted in green.

we could not detect any Ca^{2+} densities in this region in our cryo-EM structure of IP_3R1 (45). These observations indicate that conserved residues forming the Ca^{2+}-binding site in the two main families of intracellular Ca^{2+}-release channels are good candidates to mediate the regulation of IP_3R by Ca^{2+}.

Substitutions at the Putative Ca^{2+} Coordinating Residues in hIP_3R1 Diminished Agonist-Induced Ca^{2+} Release. IP_3R1 is the best-studied subtype in terms of regulation by Ca^{2+} (13, 46, 47). Therefore, we stably overexpressed WT hIP_3R1 or hIP_3R1 with substitutions at the 2002 glutamic acid (E) residue (Fig. 1*C*) to aspartate (D), alanine (A), or glutamine (Q) in HEK-3KO cells previously generated in our laboratory by CRISPR-Cas9 technology to lack native IP_3Rs (19). The rationale for the substitutions chosen being that the E-D residue change retained the side chain charge; the E-Q substitution resulted in a similar-size side chain that does not preserve the side chain charge but is still hydrophilic; and the E-A substitution maintains the β carbon moiety but has no other side chain chemistry.

When expressed in HEK-3KO cells, IP_3R1 protein levels of exogenously (exo) expressed WT hIP_3R1, hIP_3R1 E2002D, hIP_3R1 E2002A, and hIP_3R1 E2002Q stable cell lines were higher than WT HEK293 and endogenous (endo) hIP_3R1 cells previously generated in our laboratory by CRISPR-Cas9 technology to lack the other two native IP_3Rs (19) (Fig. 2 *A* and *B*). When stably expressed, all of the mutants were properly targeted

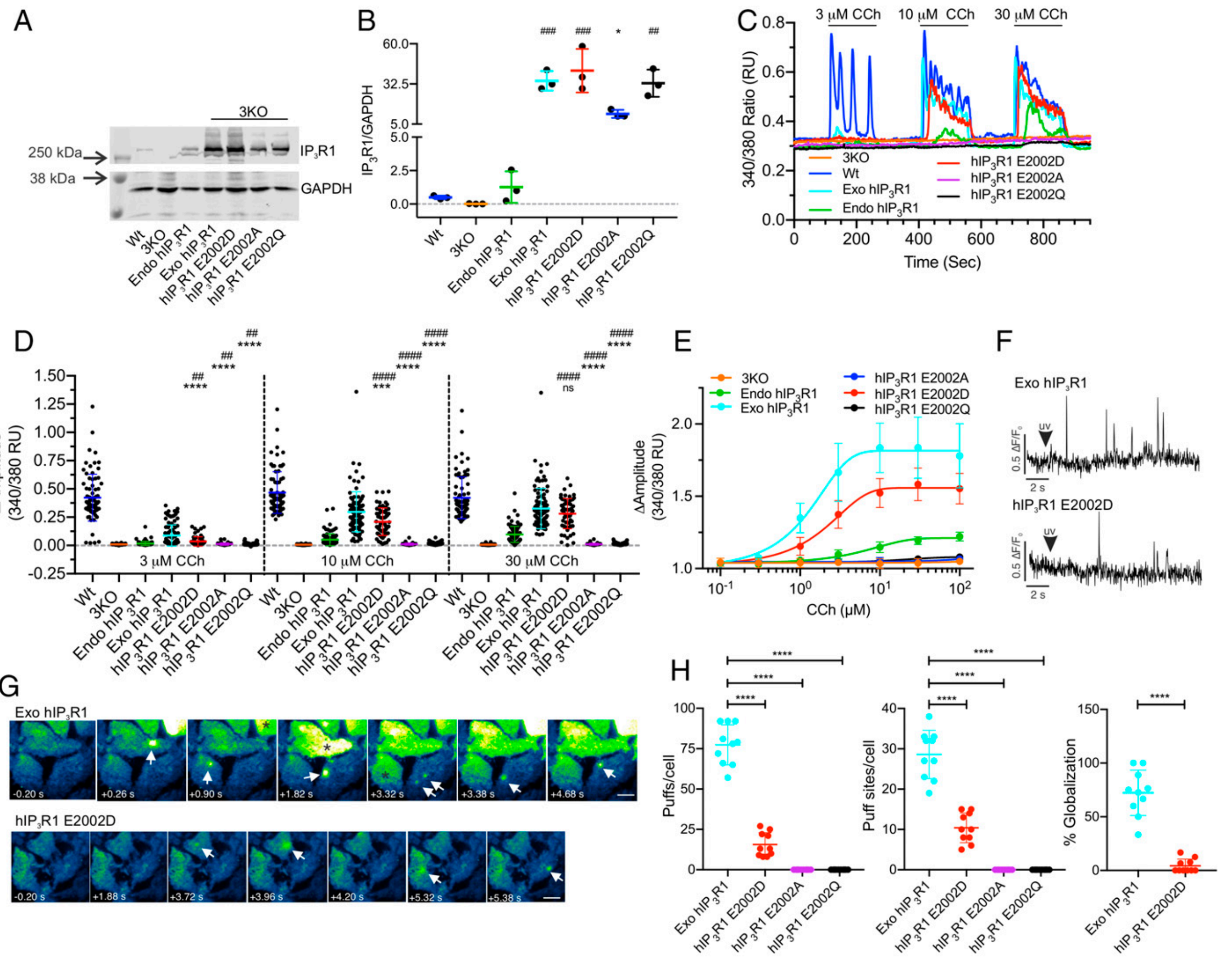

Fig. 2. Substituting E2002 with D, A, or Q residue in hIP$_3$R1 significantly diminished agonist-induced Ca^{2+} signals when stably expressed in HEK-3KO cells. Stable hIP$_3$R1 cell lines with a substitution at E2002 position to D, A, or Q were generated in HEK-3KO cells. (*A*) A representative western blot depicting IP$_3$R1 and GAPDH protein levels in WT HEK293 (Wt), HEK-3KO (3KO), HEK-2KO (lacking native IP$_3$R2 and IP$_3$R3 subtypes, endo hIP$_3$R1), 3KO cells overexpressing WT IP$_3$R1 (exo hIP$_3$R1), and E2002D/A/Q substitution (hR1 E2002D/A/Q). (*B*) Scatterplot depicting quantification of IP$_3$R1 protein level normalized to GAPDH from three independent western blots. Data are means ± SDs of three ($n = 3$) independent experiments. ##$P < 0.01$, ###$P < 0.001$ when compared to endo hIP$_3$R1 cell line and *$P < 0.05$ when compared to exo hIP$_3$R1 cell line; one-way ANOVA with Tukey's test was performed. (*C*) Representative traces showing CCh-induced (3, 10, and 30 μM) Ca^{2+} release from 3KO (orange), WT (blue), endo hIP$_3$R1 (green), exo hIP$_3$R1 (cyan), hIP$_3$R1 E2002D (red), hIP$_3$R1 E2002A (purple), and hIP$_3$R1 E2002Q (black) cells in single-cell assays. (*D*) Scatterplot summarizing change in amplitude (peak ratio – basal ratio: average of 20 ratio points immediately preceding addition) to increasing doses of CCh (3, 10, and 30 μM) for experiments similar to those shown in (*C*). Data are means ± SDs of at least three independent experiments. ##$P < 0.01$, ####$P < 0.0001$ when compared to endo hIP$_3$R1 cell line and ***$P < 0.001$, ****$P < 0.0001$ when compared to exo hIP$_3$R1 cell line; Mann-Whitney *U* test was performed. ns: not significant. (*E*) Dose-response curve showing maximum amplitude from Fura-2/AM loaded 3KO (orange), endo hIP$_3$R1 (green), exo hIP$_3$R1 (cyan), hIP$_3$R1 E2002D (red), hIP$_3$R1 E2002A (purple), and hIP$_3$R1 E2002Q (black) cells in population-based assays when treated with increasing concentrations (100 nM, 300 nM, 1 μM, 3 μM, 10 μM, 30 μM, and 100 μM) of CCh. (*F*) Representative traces of Cal-520 fluorescence ratios (ΔF/F$_0$) from the center of a single puff site (~1 × 1 μm) evoked by photolysis of ci-IP$_3$ at 2 s (indicated by arrow) in exo hIP$_3$R1 (upper trace) and hIP$_3$R1 E2002D (lower trace) cells using a TIRF microscope. (*G*) TIRFM images from exo hIP$_3$R1 (*Upper* panel) and hIP$_3$R1 E2002D (*Lower* panel) showing Ca^{2+} puffs at indicated time point. Typical of at least 10 independent experiments. Arrows indicate Ca^{2+} puffs/puff sites, and asterisks indicate globalization of Ca^{2+} signals. (*H*) Scatterplots summarizing number of puffs/cell, puff sites/cell, and % globalization in exo hIP$_3$R1 cells (cyan), hIP$_3$R1 E2002D (red), hIP$_3$R1 E2002A (purple), and hIP$_3$R1 E2002Q (black) cells ($n = 10$ cells). Data are means ± SDs of 10 ($n = 10$) independent experiments. ****$P < 0.0001$ when compared to exo hIP$_3$R1 cell line; Mann-Whitney *U* test was performed. Unless otherwise stated, all of the data above comes from at least $n = 3$ experiments.

to the ER, exhibiting a characteristic reticular expression pattern (*SI Appendix*, Fig. S2*A*). In addition, each mutant receptor ran exclusively as a tetramer on native nondenaturing gels (*SI Appendix*, Fig. S2*B*). To investigate the functional consequences of these substitutions on hIP$_3$R1 channel activity, we performed single-cell imaging assays to assess IP$_3$-induced Ca^{2+} release using carbachol (CCh) and trypsin as agonists acting via the G$_\alpha$q-coupled M3 muscarinic receptor and protease-activated receptor 2, respectively. CCh-induced Ca^{2+} release was markedly diminished in the hIP$_3$R1 E2002D cells when compared to exo hIP$_3$R1 cells at lower doses of CCh (3, 10 μM); however, such differences disappeared at a higher dose of CCh (30 μM), presumably due to the recruitment of additional IP$_3$Rs caused by Ca^{2+}-induced Ca^{2+} release at higher concentrations of CCh (Fig. 2 *C* and *D*). CCh-induced Ca^{2+} release was significantly attenuated in hIP$_3$R1 E2002A and hIP$_3$R1 E2002Q cells as compared to exo and endo hIP$_3$R1 cells at all doses of CCh (3, 10, and 30 μM) (Fig. 2 *C* and *D*). Moreover, the percentage of responding cells was also significantly lower in stable cells with substitutions at the E2002 residue compared to WT cells

(*SI Appendix*, Fig. S3*A*). Similarly, trypsin-evoked Ca^{2+} release was also significantly attenuated in cells with substitutions at the E2002 site when compared to both endo and exo hIP_3R1 cells (*SI Appendix*, Fig. S3 *C* and *D*). The HEK-3KO cells, as previously demonstrated, failed to respond to stimulation with either trypsin (*SI Appendix*, Fig. S3 *C* and *D*) (18, 19) or CCh (Fig. 2 *C*–*E*). Furthermore, in a population-based assay performed on a FlexStation3 plate reader with microfluidics, CCh-induced Ca^{2+} release as reflected by both the maximum amplitude changes (Fig. 2*E*) and area under the curve (AUC) (*SI Appendix*, Fig. S3*B*) were markedly attenuated in E2002D and decimated in E2002A and E2002Q cells when compared to both exo and endo IP_3R1 cells. These results suggest that the negative charge on the side chain residue at the 2002 position in hIP_3R1 is critical for binding to Ca^{2+}, and neutralizing this charge prevented IP_3-induced Ca^{2+} release and IP_3R1 activation.

Next, to measure the activity of the hIP_3R more directly and without the global effects on neighboring IP_3R by increasing Ca^{2+}, we investigated the effect of substitutions at the E2002 site on the fundamental Ca^{2+} signals mediated by IP_3Rs (called Ca^{2+} puffs) upon uncaging caged inositol triphosphate (ci-IP_3) using total internal reflection microscopy (TIRFM) (31, 33, 48–50). As shown in the representative traces (Fig. 2*F*) and images (Fig. 2*G*), the number of fundamental Ca^{2+} signals obtained from the hIP_3R1 E2002D cells were significantly diminished when compared to WT exo hIP_3R1 cells following the uncaging of ci-IP_3 (Movies S1 and S2). The number of puffs per cell, puff sites per cell, and the percentage of cells in which Ca^{2+} signals globalized were significantly attenuated in hIP_3R1 E2002D cells as compared to WT hIP_3R1 cells (Fig. 2*H*). The rise and fall times did not differ between these two cells (*SI Appendix*, Fig. S3*E*). We failed to detect any puffs in cells expressing hIP_3R1 with either E2002A or E2002Q, again reinforcing the importance of the negative charge at this residue in the Ca^{2+} activation site (Fig. 2*H*).

Substituting the Putative Ca^{2+} Coordinating Residue in hIP_3R3 Diminished Agonist-Induced Ca^{2+} Release. Given that this residue is identical in all human IP_3R subtypes, we postulated that if E2002 indeed represented an important charged residue for the coordination of Ca^{2+} and subsequent activity of hIP_3R1, then the functional effect of mutating this residue should be conserved in other hIP_3R subtypes. Therefore, we generated stable cell lines in HEK-3KO with substitution at the analogous E1946 residue in hIP_3R3 (Fig. 1*C*). The IP_3R3 protein levels of the hIP_3R3 E1946Q stable cell line were slightly more than the WT HEK293 and endogenous hIP_3R3 cells previously generated in our laboratory by CRISPR-Cas9 technology to lack the other two native IP_3Rs (Fig. 3 *A* and *B*). When stably expressed, hIP_3R3 E1946Q was properly targeted to the ER, exhibiting a characteristic reticular expression pattern (*SI Appendix*, Fig. S4*A*). In addition, the mutant receptor, like hIP_3R3, ran exclusively as a tetramer on native nondenaturing gels (*SI Appendix*, Fig. S4*B*). To determine the functional consequence of this substitution, as before, we performed single-cell imaging assays to assess IP_3-induced Ca^{2+} release using CCh and trypsin as agonists. While the exo hIP_3R3, endo hIP_3R3 and WT HEK293 cells responded to agonist stimulation, the hIP_3R3 E1946Q cells, like 3KO cells, did not respond to various doses of CCh (3, 10, and 30 μM) (Fig. 3 *C* and *D*). The percentage of responding cells were also significantly lower in stable cells with the E1946Q substitution as compared to WT cells (*SI Appendix*, Fig. S5*A*).

To further substantiate these results, we performed single-cell imaging experiments using trypsin (500 nM) as an agonist. A consistent lack of trypsin-induced Ca^{2+} release in hIP_3R3 E1946Q cells was observed when compared to WT stable cells (*SI Appendix*, Fig. S5 *C* and *D*). Interestingly, both the WT and endo hIP_3R3 cells, which express IP_3R3 protein levels comparable to those of hIP_3R3 E1946Q cells, responded to trypsin (*SI Appendix*, Fig. S5 *C* and *D*) and various doses of CCh (Fig. 3 *C* and *D*). Furthermore, we also performed population-based assays to determine CCh-induced Ca^{2+} release in hIP_3R3 E1946Q cells. Similar to single-cell imaging assays, CCh-induced Ca^{2+} release, as represented by the maximum amplitude changes (Fig. 3*E*) and AUC (*SI Appendix*, Fig. S5*B*), was abolished in hIP_3R3 E1946Q cells when compared to both exo and endo hIP_3R3 cells. Overall, these results indicate that the negative charge on the conserved side chain residues in both the hIP_3R1 and hIP_3R3 subtypes is critical for coordinating Ca^{2+} and the activity of hIP_3R subtypes.

Is the negative charge on the conserved side chain residues in IP_3R3 essential for Ca^{2+} binding and activity across species? To address this question, we next generated stable cell lines expressing rat IP_3R3 (rIP_3R3) WT or rIP_3R3 with E1945Q substitution in HEK-3KO cells (*SI Appendix*, Fig. S6 *A* and *B*). We performed single-cell imaging and population-based assays to determine agonist-induced Ca^{2+} release using these stable cells. Remarkably, both the CCh- (*SI Appendix*, Fig. S6 *C*–*E*) and trypsin-induced (*SI Appendix*, Fig. S6 *H* and *I*) Ca^{2+} release was decreased in rIP_3R3 E1945Q cells as compared to rIP_3R3 WT cells. A similar decrease in CCh-induced Ca^{2+} release was observed in population-based assays (*SI Appendix*, Fig. S6 *F* and *G*). To summarize, these observations indicate that the negative charge on the conserved side chain residues in IP_3Rs across multiple organisms is critical for binding to Ca^{2+} and the ensuing agonist-induced Ca^{2+} release.

Loss of Negative Charge in the Putative Ca^{2+}-Binding Pocket Shifts the Ca^{2+} Sensitivity for Activation of hIP_3R1. The previous experiments suggest strongly that negatively charged residues in a putative Ca^{2+}-binding pocket centered around E2002 are necessary for the full activity of hIP_3R, but they do not provide biophysical, mechanistic insight into how Ca^{2+} binding controls IP_3R activity. We therefore generated stable cell lines expressing WT hIP_3R1 or hIP_3R1 with substitutions at the E2002 and E1938 residues in DT40-3KO chicken lymphocytes, IP_3R null cells (*SI Appendix*, Fig. S7 *A* and *B*). Interestingly, consistent with HEK-3KO cells, neutralizing the negative charge on side chain of either of these residues significantly abrogated Ca^{2+} signals evoked by trypsin in population-based assays in DT40 cells (*SI Appendix*, Fig. S7 *C* and *D*).

Next, we performed "on-nucleus" single-channel recordings of IP_3R1 activity after exposure to IP_3 and various $[Ca^{2+}]$. As described previously, by our laboratory (51–53) and others (24, 54), at an optimum [ATP] (5 mM) and at a saturating $[IP_3]$ (10 μM), the open probability (P_o) of the hIP_3R increased with increasing $[Ca^{2+}]$; channel activity was barely evident at 10 nm Ca^{2+} and increased to reach a maximum P_o of ∼0.7 at 200 nM Ca^{2+}. Increasing $[IP_3]$ to 100 μM, failed to augment activity further. At higher $[Ca^{2+}]$, hIP_3R1 activity decreased and was essentially absent at 100 μM Ca^{2+} (Fig. 4 *A* and *G*). Similar experiments were then performed in cells expressing hIP_3R1 harboring the conservative charge mutation E2002D. While single-channel activity was reduced in cells expressing this mutation (maximal P_o ∼0.45 at 200 nM Ca^{2+}), a similar dependency on Ca^{2+} for activation and inhibition compared to WT hIP_3R1 was retained by this mutation. The decrease in overall channel activity was not due to a reduction in the

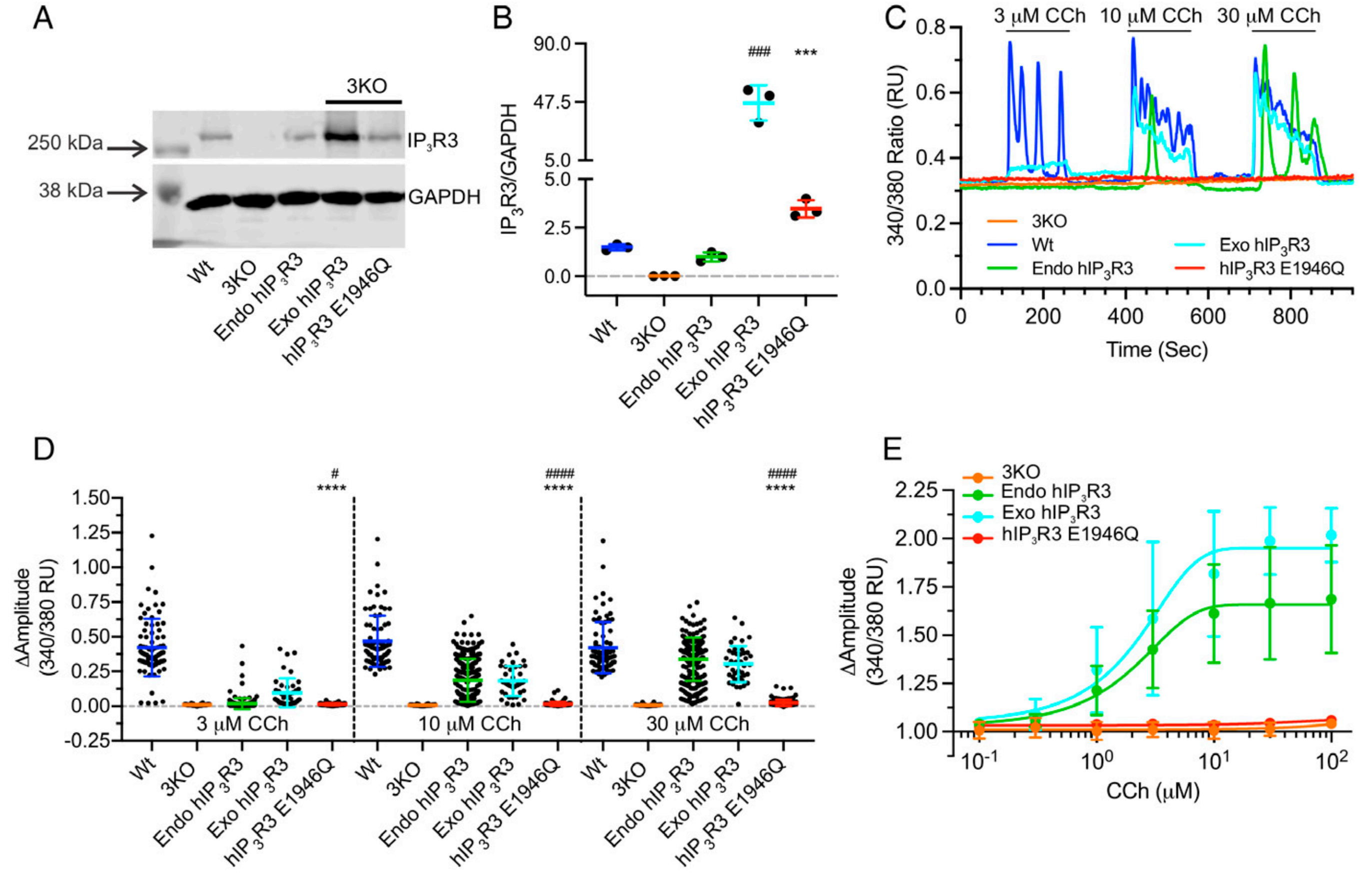

Fig. 3. Substituting E1946 with Q residue in hIP_3R3 significantly diminished agonist-induced Ca^{2+} release when stably expressed in HEK-3KO cells. Stable hIP_3R3 cells with substitution at the E1946 position to Q were generated in HEK-3KO cells. (*A*) A representative western blot depicting IP_3R3 and GAPDH protein levels in HEK293 (Wt), HEK-3KO (3KO), HEK-2KO (lacking native IP_3R1 and IP_3R2 subtypes, endo hIP_3R3), 3KO cells overexpressing WT hIP_3R3 (exo hIP_3R3), and 3KO cells overexpressing hIP_3R3 with E1946Q substitution (hIP_3R3 E1946Q). (*B*) Scatterplot depicting quantification of IP_3R3 protein level normalized to GAPDH from three independent western blots. Data are means ± SDs of three ($n = 3$) independent experiments. ###$P < 0.001$ when compared to endo hIP_3R3 cell line and ***$P < 0.001$ when compared to exo hIP_3R3 cell line; one-way ANOVA with Tukey's test was performed. (*C*) Representative traces showing CCh-induced (3, 10, and 30 μM) Ca^{2+} release from 3KO (orange), Wt (blue), endo hIP_3R3 (green), exo hIP_3R3 (cyan), and hIP_3R3 E1946Q (red) cells in single-cell assays. (*D*) Scatterplot summarizing change in amplitude (peak ratio – basal ratio: average of 20 ratio points immediately preceding addition) to increasing doses of CCh for experiments similar to those shown in (*C*). WT and 3KO data from Fig. 2*D* is shown for comparison. Data are means ± SDs of three ($n = 3$) independent experiments. #$P < 0.05$, ####$P < 0.0001$ when compared to endo hIP_3R3 cell line and ****$P < 0.0001$ when compared to exo hIP_3R3 cell line; Mann-Whitney *U* test was performed. (*E*) Dose-response curve showing change in maximum amplitude from Fura-2/AM loaded 3KO (orange), endo hIP_3R3 (green), exo hIP_3R3 (cyan), and hIP_3R3 E1946Q (red) cells in population-based assays when treated with increasing concentrations (100 nM, 300 nM, 1 μM, 3 μM, 10 μM, 30 μM, and 100 μM) of CCh. Unless otherwise stated, all of the data above comes from at least $n = 3$ experiments.

sensitivity to IP_3, as increasing IP_3 to 100 μM had no further effect on hIP_3R1 P_o (Fig. 4 *B* and *G*).

Next, we investigated the consequences of substitution of E2002 to alanine. Strikingly, no IP_3R activity was evident at $[Ca^{2+}]$ in a range that resulted in enhanced P_o in WT hIP_3R1 (10 to 200 nM Ca^{2+}). IP_3R activity, albeit reduced in comparison to the hIP_3R1 retaining negative charge at this residue, was observed at 1 μM, which was further enhanced by increasing $[Ca^{2+}]$ to 3 μM and then subsequently reduced as $[Ca^{2+}]$ was increased further (Fig. 4 *C* and *G*). Again, increasing the $[IP_3]$ to 100 μM failed to increase overall activity at optimum $[Ca^{2+}]$ for this mutation. The decreased sensitivity to activation by Ca^{2+} can be readily observed in the pooled data presented in Fig. 4*G* and insert. Notably, the $[Ca^{2+}]$ required for the inhibition of activity was largely unaltered by this substitution. We failed to record any single-channel activity when E2002 was mutated to glutamine. Importantly, the current-voltage relationship for each mutant was essentially identical, indicating that the single-channel conductance of each mutant was unchanged (Fig. 4*F*).

As previously reported, the IP_3R1 exhibits modal gating; increased activity is associated with increased bursting activity (51). An increase in Ca^{2+} flux is not associated with a change in open or closed times within the burst, but an increase in the duration of bursts (*SI Appendix*, Fig. S8 *A*–*C*). We observed that fundamental gating characteristics were not altered in any of the mutations. An increase in $[Ca^{2+}]$ both increased the burst length and concomitantly decreased the interburst interval. These data indicate that an increase in IP_3R1 activity by Ca^{2+} is primarily associated with a destabilization of a long-closed state, while the attenuation of IP_3R1 activity by Ca^{2+} is associated with a transition to and stabilization of this long-closed state (*SI Appendix*, Fig. S8 *C*–*G*).

We also generated DT40-3KO cell lines stably expressing similar mutations at E1938 (*SI Appendix*, Fig. S7 *A* and *B*), which is predicted to be an additional negatively charged residue essential for coordinating Ca^{2+} in the Ca^{2+}-sensing site (Fig. 1). In a fashion similar to that of mutations in E2002, conservation of charge by the substitution of E1938 for D in hIP_3R1 resulted in a decrease in the maximum overall channel activity, with no change in the absolute sensitivity to IP_3, but the relationship for activation and inhibition of channel activity by Ca^{2+} was retained; a maximal P_o was attained at 200 nm Ca^{2+}, which subsequently decreased at a $[Ca^{2+}]$ >1 μM (Fig. 4 *D* and *G*). IP_3R1 activity in

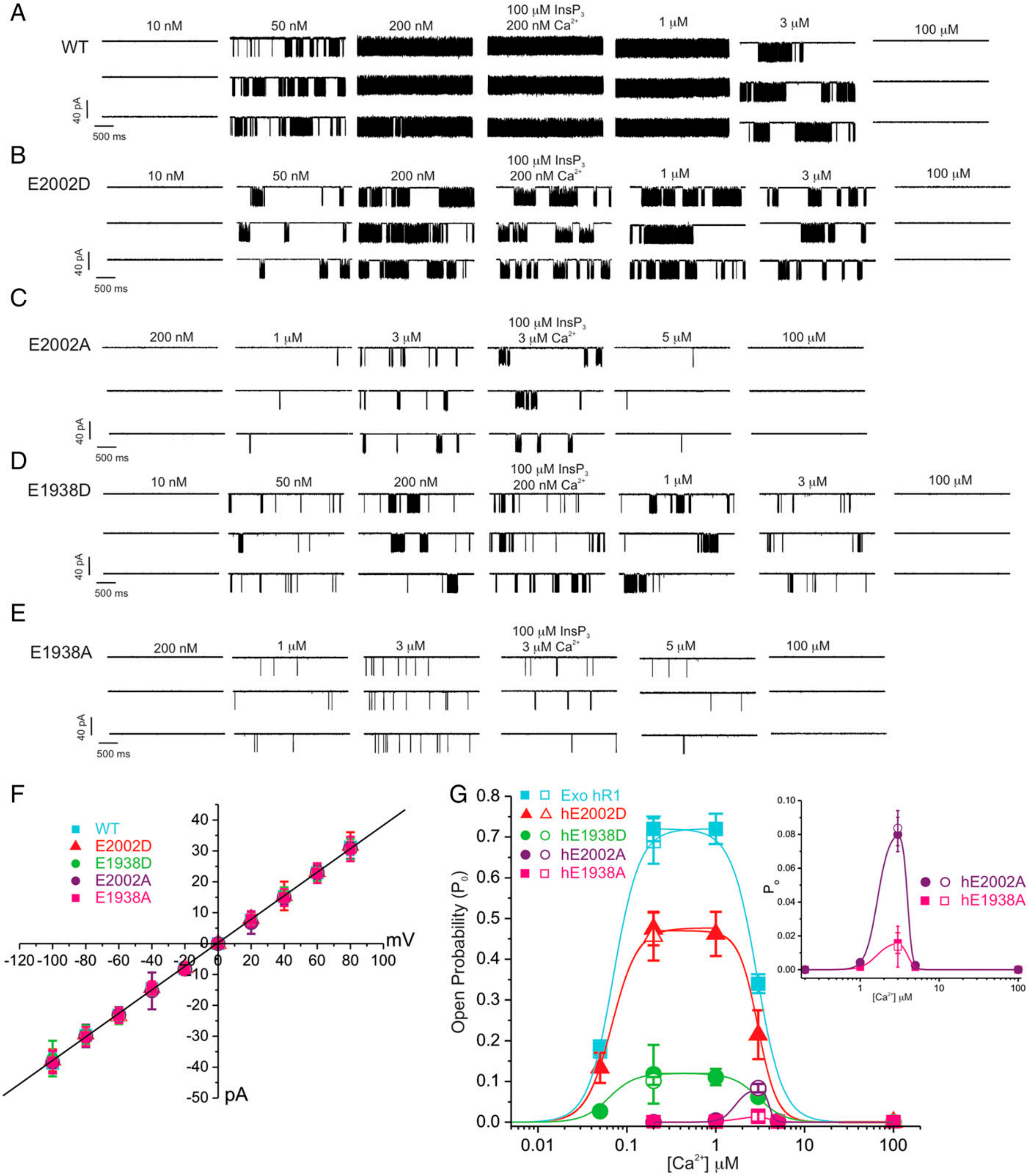

Fig. 4. Importance of negative charges in Ca^{2+} sensor site for regulation of hIP_3R1 by Ca^{2+}. The activity of WT hIP_3R1 and mutants was monitored in the "on-nucleus" configuration in DT40-3KO cells stably expressing the indicated constructs as detailed in *Materials and Methods*. (*A*) Representative sweeps are shown at the indicated $[Ca^{2+}]$ stimulated by 10 μM IP_3 (unless stated otherwise) in the presence of optimal ATP for WT hIP_3R1. Maximal activity is observed at 200 nM^{-1} μM Ca^{2+} and then subsequently decreases. Maximal P_o was not increased by increasing $[IP_3]$ to 100 μM. (*B*) Representative activity is shown for E2002D hIP_3R1. The maximal P_o at each $[Ca^{2+}]$ is reduced compared with WT hIP_3R1, but the regulation by increasing Ca^{2+} mirrors that seen with WT hIP_3R1. (*C*) Representative activity is shown for E2002A hIP_3R1. Maximal P_o is markedly reduced and the $[Ca^{2+}]$ where maximum activity is observed is right shifted to higher $[Ca^{2+}]$. Inhibition of IP_3R activity occurs at similar $[Ca^{2+}]$ to WT hIP_3R1. (*D*) Representative activity is shown for E1938D hIP_3R1. In a fashion similar to that of E2002D, the maximal P_o at each $[Ca^{2+}]$ is reduced compared with WT hIP_3R1, but the regulation by increasing Ca^{2+} mirrors that seen with WT hIP_3R1. (*E*) Representative activity is shown for E1938A hIP_3R1. In a fashion similar to that of E2002A, maximal P_o is markedly reduced and the $[Ca^{2+}]$ where maximum activity is observed is right shifted to higher $[Ca^{2+}]$. Inhibition of IP_3R activity occurs at similar $[Ca^{2+}]$ to WT hIP_3R1. (*F*) Current versus voltage relationship for the WT (Exo hR1) and mutant hIP_3R1 channels generated at 10 mM and optimal $[Ca^{2+}]$ for each construct. (*G*) Pooled data. Solid symbols: recordings obtained using 10 μM IP_3 at indicated Ca^{2+} concentrations from Exo hR1 (Exo hIP_3R1: cyan), hE2002D (red), hE1938D (green), hE2002A (purple), and hE1938A (pink). Open symbols: recordings obtained using 100 μM IP_3 at an optimal Ca^{2+} concentration (200 nM). Inset shows pooled data for alanine mutations with an expanded y axis.

cells expressing hIP_3R1 E1938A again displayed a right-shifted, decreased sensitivity to Ca^{2+}, similar to E2002A, with maximum activity observed at 3 μM Ca^{2+} before subsequently decreasing (Fig. 4 *E* and *G*). Similar to E2002D, the inhibition of activity characteristic of higher [Ca^{2+}] was largely unaltered when compared to WT hIP_3R1. In total, these data are consistent with E2002 and E1938 comprising key Ca^{2+}-binding residues responsible for the activation phase of the bell-shaped Ca^{2+} relationship underlying IP_3R activity.

Discussion

The regulation of IP_3R induced Ca^{2+} release by Ca^{2+} was recognized early. Initial studies reported that IP_3-induced Ca^{2+} release from the ER was inhibited by Ca^{2+} (55, 56). Subsequently, a series of seminal studies reported that increasing [Ca^{2+}] first positively potentiates IP_3R activity and then at higher concentrations reduces channel activity, resulting in the characteristic bell-shaped regulation of IP_3-induced Ca^{2+} release and channel activity, which is thought to be pivotally important for the spatiotemporal control of Ca^{2+} release (8, 20, 22, 24, 57–60). Ongoing studies have since investigated whether this fundamental regulation is directly through the interaction with motifs in the IP_3R protein itself, or through an accessory protein. For example, single-channel experiments in which [Ca^{2+}] can be rigorously controlled on both faces of the channel indicate that IP_3R activity appears to be regulated by changes in [Ca^{2+}]$_i$ close to the open channel pore, as opposed to the [Ca^{2+}] in the ER lumen (29).These data make it improbable that potential Ca^{2+} binding site(s) on the luminal face of IP_3Rs contribute to activation. Moreover, the failure to detect any interactions between Ca^{2+}-binding proteins and IP_3Rs as a function of changes in the [Ca^{2+}] makes it unlikely that Ca^{2+} sensitivity is conferred through an interaction with a binding partner (61). Taken together, these findings strongly indicate that the Ca^{2+} binding site(s) lie within the receptor.

In terms of known Ca^{2+}-binding motifs, IP_3Rs lack a canonical EF hand, C2 domain, or other conventional Ca^{2+}-binding motifs (27); however, Ca^{2+} binds to several linear fragments spread across various domains (35, 36). Of note, rIP_3R1 (residues 1,961 to 2,219) and rIP_3R2 (residues 1,914 to 2,173) coupling domain fragments expressed as recombinant proteins in bacteria are strongly bound to $^{45}Ca^{2+}$ (61). Nevertheless, residues coordinating Ca^{2+} in the IP_3R that are responsible for modulating activity have not been functionally described. Recently, by comparing cryo-EM structures of RyR obtained in the presence and absence of its activating ligands (Ca^{2+}/ATP/caffeine), putative amino acids residues forming the Ca^{2+}-activating site were identified (40). Moreover, mutational analysis experimentally confirmed that these residues confer Ca^{2+} sensitivity to the RyR channel (41). Cryo-EM structures of RyR resolved in the presence of Ca^{2+} revealed that the pore remained open, consequently permitting the flow of Ca^{2+} ions from the ER to the cytoplasm (40). As noted, the key residues forming the putative Ca^{2+} sensor site in IP_3R1 (45), hIP_3R2 and hIP_3R3, are perfectly conserved and similar to the Ca^{2+}-activating site identified in human RyRs (Fig. 1). Moreover, Ca^{2+}-binding residues at this activating site in RyR and IP_3Rs are identical in a number of species representing mammals, fish, and birds and also highly conserved in some lower order organisms (Fig. 1 and *SI Appendix*, Fig. S1*A*). This conservation, together with our mutagenesis in IP_3R subtypes from two species, makes it highly likely that this Ca^{2+} sensor region represents the Ca^{2+} activation site in at least all mammalian IP_3R and RyR subtypes. Nevertheless, even though these residues are evolutionarily well conserved, IP_3Rs in *Capsaspora owczarzaki*, paradoxically, appears not to be regulated by Ca^{2+} in a manner similar to mammalian IP_3R (62) and thus, this may indicate that other structural elements required for allosteric regulation of activity by Ca^{2+} are absent in this species. Interestingly, in *Drosophila melanogaster*, a point mutation (wc703, G2117E; G2123 in variant used in *SI Appendix*, Fig S1*A*) in the calcium sensor region of IP_3R caused an increase in the Ca^{2+}-binding affinity/sensitivity and open probability of the channel (63, 64). The glutamate residue in this gain-of-function mutation may stabilize Ca^{2+} coordination in the Ca^{2+}-activating site, thereby augmenting the Ca^{2+} sensitivity of IP_3R. In the hIP_3R3 structure, the HD/ARM2 putative Ca^{2+} binding site was poorly resolved (15). This site, while conserved in IP_3R subtypes, is not present in RyRs (*SI Appendix*, Fig. S1*B*), and we could not detect any Ca^{2+} densities at this site in our cryo-EM structures (45). Any role for the site in the regulation of IP_3R activity should be the subject of further investigation.

In the present study, based on striking similarities between RyRs and IP_3Rs structures at the putative Ca^{2+} sensor site, we generated several stable cell lines in HEK-3KO and DT40-3KO cells (lacking all three native IP_3Rs) expressing hIP_3R1, hIP_3R3, and rIP_3R3 with substitutions at conserved amino acid residues forming the Ca^{2+} sensor site (Figs. 2 and 3 and *SI Appendix*, Figs. S6 and S7). We then interrogated the channel properties of these mutants when compared to their WT counterparts. A common concern associated with taking a mutagenesis approach to studying structure-function relationships is that mutations may grossly alter the structure of the protein in a manner unrelated to the targeted disruption. While this cannot be unequivocally ruled out without a high-resolution structure of each mutant, the observation that the mutants formed tetrameric structures that were properly localized to the ER argues against a major disruption in the protein structure (*SI Appendix*, Figs. S2 and S4). This idea is further reinforced by data demonstrating that the single-channel conductance (Fig. 4*F*) and gating characteristics of the mutants (*SI Appendix*, Fig. S8), indicative of the structure of the pore and the ability of conformational changes in the protein to open the pore, were identical to WT IP_3R. Agonist-induced Ca^{2+} release was significantly reduced when the glutamic acid residue at position 2002 in hIP_3R1 was substituted for the native aspartate residue (Fig. 2 and *SI Appendix*, Fig. S3) at this position, indicating that disruption of the structure of the putative binding pocket following reduction in the size of the residue, without altering charge, disrupted Ca^{2+} regulation of IP_3R activity. Furthermore, agonist-induced Ca^{2+} release was completely abrogated upon neutralizing the negative charge on the glutamic acid side chain residue at the 2002 position by substitution with either glutamine or alanine (Fig. 2 and *SI Appendix*, Fig. S3), indicating that the negative charge of this residue is pivotal for activity. Similar data were obtained in DT40 cells upon neutralizing negative charge on side chain residue at either E2002 or E1938 residue in hIP_3R1 (*SI Appendix*, Fig. S7).

Recent technological advances, using high-speed TIRFM, allow near-electrophysiological measurement of the biophysical characteristics of fundamental Ca^{2+} signals arising from a cluster of IP_3Rs called Ca^{2+} puffs (31, 48, 65–68). Consistent with the effect on global Ca^{2+} signals, Ca^{2+} puffs were also significantly diminished in E2002D cells or completely abrogated in E2002A and E2002Q cells (Fig. 2 *F*–*H*). Notably, while diminished in number, Ca^{2+} puffs in cells expressing E2002D retained the kinetics of WT IP_3R1 consistent with this mutant retaining its bell-shaped modulation by Ca^{2+} (Fig. 4G). Similarly, the substitution of glutamine for glutamic acid at the analogous 1946 position in hIP$_3$R3 also decimated agonist-induced Ca^{2+} release (Fig. 3 and *SI Appendix*, Fig. S5). A similar result was obtained upon mutating the analogous residue in rIP$_3$R3 (*SI Appendix*, Fig. S6). We did not consider substitution of multiple Ca^{2+} coordinating residues in a site to avoid excessive perturbations in the native structure of IP$_3$Rs.

Our single-channel data provide unparalleled mechanistic insight into how the binding of Ca^{2+} to the Ca^{2+} sensor site influences the activity of the IP$_3$R. Mutation of either E2002 or E1938 by substitution with an aspartate acid residue (Fig. *B* and *D*) or an alanine residue (Fig. 4 *C* and *E*) did not alter the single-channel conductance (Fig. 4*F*) or the modal gating of the channel in bursts (*SI Appendix*, Fig. S8). Notably, however, mutation of these residues with either substitution had marked effects on channel P$_o$, and, most strikingly, the loss of negative charge markedly altered the activation of channel activity by Ca^{2+} without altering the inhibition at higher [Ca^{2+}] (Fig. 4 *A*–*E*). This is most clearly appreciated by comparing the pooled activity relationships for WT hIP$_3$R1 with the charge-conserved aspartic acid substitutions at either site with the mutations to alanine (Fig. 4*G*). Clearly, while the activity of the aspartic acid (Fig. 4 *B* and *D*)–substituted mutants are reduced compared to WT hIP$_3$R1 (Fig. 4*A*), the activity is regulated with an identical bell-shaped relationship (Fig. 4*G*). In contrast, the alanine mutants have further reduced maximum activity, but peak activation is achieved at higher [Ca^{2+}] when compared to WT or glutamic acid–harboring mutants (Fig. 4 *C* and *E*). The reduction in overall activity of each mutant compared to WT is consistent with disruption of the overall integrity of the Ca^{2+}-binding pocket by alteration in the size and charge of side chains resulting in disordered transduction of conformational changes in Ca^{2+} binding to gating of the pore. Primarily, these data further reinforce that the negative charge on both amino acid residues E2002 and E1938 are critically important for coordinating Ca^{2+} in the Ca^{2+} sensor site, which leads to the activation of IP$_3$R.

Given that each protomer contributes one Ca^{2+} binding site in the tetrameric IP$_3$R assembly, a remaining important question relates to the stoichiometry of Ca^{2+} binding necessary for activation. Ca^{2+} activation of IP$_3$R single-channel activity is generally reported to be modestly positively cooperative (21), which may suggest that binding of more than a single Ca^{2+} activates the channel. We envision that a concatenated receptor approach with increasing numbers of subunits harboring Ca^{2+} binding site mutants will be used to elucidate how many Ca^{2+} are necessary to open the channel (19). In addition, as IP$_3$R subtypes are differentially modulated by IP$_3$, ATP, and activation by Ca^{2+} and overall activity is determined by the interplay between these regulatory inputs (21, 25, 52, 53, 69), whether the effects of Ca^{2+} binding are distinct in the context of particular IP$_3$R subtypes or heterotetrametric assemblies should be determined. Further work is also necessary to elucidate the structural basis of inhibition of IP$_3$R activity by Ca^{2+}.

Materials and Methods

Plasmid Constructs. Substitutions to amino acids D, A, or Q at the desired site/residue in rIP$_3$R3, hIP$_3$R3, and hIP$_3$R1 were generated using *Pfu* Ultra II Hotstart 2X Master Mix (Agilent Technologies) and appropriate primers obtained from Integrated DNA Technologies (*SI Appendix*, Table S1). A QuikChange Lightning site-directed mutagenesis kit (Agilent Technologies #210518) was used to introduce the desired substitution in cDNAs encoding the rIP$_3$R3 (NP_037270), hIP$_3$R3 (NP_002215.2), and hIP$_3$R1 (NP_001093422.2) in pDNA3.1 expression plasmid using mutagenic primers. The introduction of desired substitution and coding regions for all of the constructs was confirmed by Sanger sequencing.

Alignment of IP$_3$R Protein Sequences from Various Organisms. Alignment of IP$_3$R protein sequences from *Rattus norvigecus*–short IP$_3$R1 (used in Fig. 1*C*) (P29994.2), IP$_3$R1 (NP_001257525.1) (used in *SI Appendix*, Fig. S1), IP$_3$R2 (NP_112308.1), and IP$_3$R3 (NP_037270.2); *Homo sapiens*–IP$_3$R1 (NP_001093422.2), IP$_3$R2 (NP_002214.2), IP$_3$R3 (NP_002215.2), RyR1 (NP_000531.2), RyR2 (NP_001026.2), and RyR3 (NP_001027.3); *Capsaspora owczarzaki*–IP$_3$RA (XP_004347577.1); *Caenorhabditis elegans*–IP$_3$R1 (NP_001023170.1); *Drosophila melanogaster*–IP$_3$R (NP_730941.1); *Danio rerio*–IP$_3$R1 (XP_021335554.1); *Gallus gallus*–IP$_3$R1 (NP_001167530.1); *Mus musculus*–IP$_3$R1 (NP_034715.3); *Bos taurus*–IP$_3$R1 (NP_777266.1); *Canis familiaris*–IP$_3$R1 (XP_005632286.1); *Macaca mulatta*–IP$_3$R1 (NP_034715.3); and *Pan troglodytes*–IP$_3$R1 (XP_009443057.1) were generated using GeneDoc.

Cell Culture, Transfection, and Generation of Stable Cell Lines. DT40-3KO, chicken B lymphocyte cells engineered through homologous recombination for the deletion of all of the three-native endogenous IP$_3$R isoforms (70), were cultured in RPMI 1640 media supplemented with 1% chicken serum, 10% fetal bovine serum, 100 U/mL penicillin, and 100 μg/mL streptomycin in an incubator set to 39 °C with 5% CO$_2$. Transfections in DT40-3KO were performed as previously described (71). In brief, 5 million cells were washed with phosphate-buffered saline (PBS) and electroporated with 4 to 6 μg of appropriate plasmid construct using an Amaxa cell nucleofector (Lonza Laboratories) and nucleofection reagent (362.88 mM ATP-disodium salt, 590.26 mM MgCl$_2$ 6.H$_2$O, 146.97 mM KH$_2$PO$_4$, 23.81 mM NaHCO$_3$, and 3.7 mM glucose at pH 7.4). Following transfection, the cells were allowed to recover for 24 h and were subsequently transferred into 96-well plates containing media supplemented with 2 mg/mL G418. Next, 10 to 14 d after transfection, clones expressing the desired construct were expanded and subsequently screened by western blotting. Cell lines stably expressing the construct were used in further experiments.

HEK-3KO and HEK293 cells engineered in our laboratory using CRISPR-Cas technology for the deletion of all of the three-native endogenous IP$_3$R isoforms (19) were cultured in Dulbecco's modified Eagle's medium supplemented with 10% fetal bovine serum, 100 U/mL penicillin, and 100 μg/mL streptomycin in an incubator set to 37 °C with 5% CO$_2$. Transfections of the appropriate plasmid construct were performed using a previously described protocol (19). In brief, 1 million cells were washed with PBS and electroporated with 5 to 10 μg appropriate plasmid using Amaxa cell nucleofector kit T (Lonza Laboratories). Cells were allowed to recover for 48 h, and subsequently subcultured into new 10 cm^2 plates containing media supplemented with 1.5 to 2 mg/mL G418. Following 7 d of selection, individual colonies of cells were picked and transferred to new 24-well plates containing media supplemented with 1.5 to 2 mg/mL G418. Clonal lines were expanded and those expressing the desired constructs were confirmed by western blotting (18). All of the experiments using HEK cell lines were approved by the University of Rochester Institutional Biosafety Committee (GNT-Yule-15-007 rev0821).

Western Blotting. For western blotting, total protein was isolated from indicated control and stable cell lines using membrane-bound extraction buffer (10 mM Tris·HCl, 10 mM NaCl, 1 mM ethylene glycol tetraacetic acid (EGTA), 1 mM ethylenediaminetetraacetate, 1 mM NaF, 20 mM Na$_4$P$_2$O$_7$, 2 mM Na$_3$VO$_4$, 1% Triton X-100 (vol/vol), 0.5% sodium deoxycholate [wt/vol], and 10% glycerol) supplemented with protease inhibitors (Roche). Briefly, for protein isolation, following the addition of an appropriate amount of lysis buffer, cells were harvested in 1.5-mL tubes and placed on ice for 30 min. To disrupt the pellet, the tubes were vortexed for 10 s every 10 min and returned on ice. Following incubation on ice, the cell lysates were centrifuged at 13,000 rpm at 4 °C for 10 min. The supernatant was transferred to new labeled tubes. Protein concentration in the lysates was estimated using the D$_c$ protein assay kit (Bio-Rad). Equal amounts of lysates were then subjected to sodium dodecyl sulfate-polyacrylamide gel electrophoresis (SDS-PAGE) and transferred to a nitrocellulose membrane. The membranes were incubated with the indicated primary antibodies and appropriate secondary antibodies before imaging with an Odyssey infrared imaging system (LICOR Biosciences). Band intensities were quantified using Image Studio Lite version 5.2 and presented as ratios of IP$_3$R to glyceraldehyde 3-phosphate dehydrogenase

(GAPDH). The IP$_3$R1 antibody (#ARC154, Antibody Research Corporation) was used at a 1:1,000 dilution, IP$_3$R3 antibody (#610313, BD Transduction Laboratories) was used at a 1:1,000 dilution, GAPDH (#AM4300, Invitrogen) was used at a 1:75,000 dilution, and secondary goat anti-rabbit (SA535571, Invitrogen) and secondary goat anti-mouse (SA535521, Invitrogen) antibodies were used at a 1:10,000 dilution (67).

Native Blue PAGE Analysis. HEK-3KO and stable cell lines expressing WT or mutant IP$_3$R1/3 constructs were lysed in CHAPS lysis buffer supplemented with protease inhibitors (Roche). After 15 min on ice, cell lysates were cleared by centrifugation at 13,000 rpm for 10 min at 4 °C. Next, 15 μg cleared lysates were mixed with 4X sample buffer (BN2003, Invitrogen) and 5% G-250 sample additive (BN2004, Invitrogen). Samples were separated at 4 °C on a 3 to 12% Native PAGE Novex (BN2011BX10, Invitrogen) at 150 V for 1.5 h using dark cathode buffer and then at 250 V for 1 h using light cathode buffer (BN2007, Invitrogen) in the inner chamber with anode buffer in the outer chamber. Separated proteins were transferred onto polyvinylidene difluoride membrane using NuPAGE Transfer buffer (NP0006-1, Invitrogen) overnight at 4 °C. Appropriate primary and secondary antibodies were used to detect IP$_3$R1/3 complexes, as indicated for western blotting. Molecular weight markers are based on the mobility of unstained protein standard (LC075, Invitrogen).

Immunocytochemistry and Confocal Microscopy. HEK-3KO and HEK-3KO cells stably expressing WT and mutant IP$_3$R1/3 constructs were plated on poly-D-lysine (100 μg/mL)-coated coverslips. At roughly 50% confluent, cells were fixed using 4% parafomaldehyde at room temperature for 10 min. Subsequently, coverslips were washed with PBS, and cells were blocked in 10% bovine serum albumin (BSA) for 1 h. Following blocking, cells were incubated in primary antibody against IP$_3$R3 (BD Transduction) and IP$_3$R1 (#ARC154, Antibody Research Corporation) overnight at 4 °C. The following day, the primary antibody was removed, and coverslips were washed 3 times with PBS for 10 min with gentle rocking. Subsequently, the appropriate secondary antibody conjugated to Alexa Fluor 488 (Invitrogen) was incubated for 1 h at room temperature with gentle rocking. After incubation, coverslips were washed with PBS and mounted on slides. After allowing slides to dry, coverslips were sealed onto slides and imaged using confocal microscopy using an Olympus Fluoview 1000 microscope.

Measurement of Cytosolic Ca^{2+} in Intact Cells. Population-based Ca^{2+} imaging in the indicated cell lines was performed as described previously (18, 67). Briefly, adherent cells were plated in 10 cm^2 cell culture dishes. Upon attaining 90 to 100% confluency, the cells were loaded with 4 μM Fura-2/AM in cell culture media and incubated at 37 °C in the dark for 1 h. The cells were subsequently washed 3 times with imaging buffer (10 mM HEPES, 1.26 mM Ca^{2+}, 137 mM NaCl, 4.7 mM KCl, 5.5 mM glucose, 1 mM Na$_2$HPO$_4$, and 0.56 mM MgCl$_2$, at pH 7.4). An equal number (300,000 cells/well) of cells were seeded into each well of a black-walled 96-well plate. In contrast, suspended cells were cultured in 75 cm^2 flasks, pelleted and washed once with imaging buffer before counting. An equal number (500,000 cells/well) of cells were incubated with 4 μM Fura-2/AM in imaging buffer at room temperature for 1 h with constant rocking. Subsequently, the cells were pelleted and washed twice before being seeded into wells of a black-walled 96-well plate. The cells were centrifuged at 200 × *g* for 2 min to plate the bottom of the wells and incubated at appropriate temperature for 30 min before imaging. Fura-2/AM imaging was carried out by alternatively exciting the loaded cells between 340 and 380 nm; emission was monitored at 510 nm using FlexStation 3 (Molecular Devices). Data were exported to Microsoft Excel, where the peak response to increasing concentrations of agonist (0.1 to 100 μM CCh or 0.01 to 3 μM trypsin) was determined by calculating the 340/380 ratio and normalizing it to the average of the first 5 data points of the experiment (the basal Ca^{2+} value). AUC was calculated in GraphPad Prism 8 as increases above baseline that are >10% of the distance from the minimum to the maximum Y using the 5 data points before agonist addition as the baseline. Curve fitting was performed using a logistic dose-response equation in GraphPad Prism 8. Data were reported as triplicates from at least three individual plates.

Single-cell Ca^{2+} imaging in indicated cell lines was performed as described previously. Briefly, cells were seeded on 15-mm glass coverslips in 12-well plates and left undisturbed overnight. Once attached to the coverslip, the cells were washed with imaging buffer before attachment of the glass coverslip to a Warner perfusion chamber using vacuum grease. Subsequently, the cells were loaded with 2 μM Fura-2/AM for 25 min in the dark at room temperature. Cells were then perfused with imaging buffer and stimulated with indicated concentrations of CCh or trypsin. Ca^{2+} imaging was performed using an inverted epifluorescence Nikon microscope equipped with a 40× oil immersion objective. Fura-2/AM imaging was carried out by alternatively exciting the loaded cells between 340 nm and 380 nm; emission was monitored at 505 nm. Images were captured every second with an exposure of 20 ms and 4 × 4 binning using a digital camera driven by TILL Photonics software as previously described (18). Image acquisition was performed using TILLvisION software and data were exported to Microsoft Excel, where data were analyzed for change in peak amplitude and percentage of cells with predefined peak amplitudes. Each experiment was repeated at least three times.

Detection and Analysis of Ca^{2+} Puffs Using TIRFM. Stable hIP$_3$R1 exogenous WT cells or cells with substitutions at the E2002 site were cultured on 15-mm glass coverslips coated with poly-D-lysine (100 μg/mL) in a 35-mm dish for 36 h. Before imaging, the cells were washed three times with imaging buffer. The cells were subsequently incubated with Cal520-AM (5 μM; AAT Bioquest #21130) and ci-IP$_3$/PM (1 μM, Tocris #6210) in imaging buffer with 0.01% BSA in the dark at room temperature. After 1-h incubation, the cells were washed 3 times with imaging buffer and incubated in imaging buffer containing EGTA-AM (5 μM, Invitrogen #E1219). After 45 min of incubation, the media was replaced with fresh imaging buffer and incubated for an additional 30 min at room temperature to allow for the de-esterification of loaded reagents.

Following loading, the coverslip was mounted in a chamber and imaged using an Olympus IX81 inverted TIRFM equipped with oil-immersion PLAPO OTIRFM 60× objective lens/1.45 numerical aperture. Olympus CellSens Dimensions 2.3 (Build 189987) software was used for imaging. The cells were illuminated using a 488-nm laser to excite Cal-520 and the emitted fluorescence was collected through a band-pass filter by a Hamamatsu ORCA-Fusion complementary metal oxide semiconductor camera. The angle of the excitation beam was adjusted to achieve TIRF with a penetration depth of ∼140 nm. Images were captured from a final field of 86.7 × 86.7 μm (400 × 400 pixels, 1 pixel = 216 nm) at a rate of ∼50 frames/second (binning 2 × 2) by directly streaming into random access memory. To photorelease IP$_3$, ultraviolet (UV) light from a laser was introduced to uniformly illuminate the field of view. Both the intensity of the UV flash and the duration (1 s) for uncaging IP$_3$ were optimized to prevent spontaneous puffs in the absence of loaded ci-IP$_3$. Images were exported as .vsi files. Images, 5 s before and 60 s after flash photolysis of ci-IP$_3$, were captured, as described previously (67).

The .vsi files were converted to .tif files using Fiji and further processed using FLIKA, a Python programming-based tool for image processing (72). From each recording, ∼100 frames (∼2 s) before photolysis of ci-IP$_3$ were averaged to obtain a ratio image stack (F/Fo) and standard definition for each pixel for recording up to 13 s following photolysis. The image stack was Gaussian filtered, and pixels that exceeded a critical value (1.0 for our analysis) were located. The "Detect-puffs" plug-in was used to detect the number of clusters (puff sites), number of events (number of puffs), and the amplitudes and durations of localized Ca^{2+} signals from individual cells. All of the puffs identified automatically by the algorithm were manually confirmed before analysis. The results from FLIKA were saved to Microsoft Excel and graphs were plotted using GraphPad Prism 8 (73).

Preparation of DT40 Cell Nuclei. Isolated DT40 nuclei were prepared using homogenization. The homogenization buffer (HB) contained 250 mM sucrose, 150 mM KCl, 3 mM 2-mercaptoethanol (β-ME), 10 mM Tris, 1 mM phenylmethanesulphonylfluoride, pH 7.5, with a complete protease inhibitor tablet (Roche). Cells were washed and resuspended in HB before nuclear isolation using an RZR 2021 homogenizer (Heidolph Instruments) with 15 strokes at 1,200 rpm. A 3-μL aliquot of nuclear suspension was placed in a 3-mL bath solution, which contained 140 mM KCl, 10 mM HEPES, 500 μM BAPTA (1,2-bis(*o*-aminophenoxy)ethane-*N*,*N*,*N′*,*N′*-tetraacetic acid), and 246 nM free Ca^{2+}, pH 7.1. Nuclei were allowed to adhere to a plastic culture dish for 10 min before patching.

On-Nuclei Patch-Clamp Experiments. Single IP_3R channel potassium currents (i_k) were measured in the on-nucleus patch-clamp configuration using pCLAMP 9 and an Axopatch 200B amplifier (Molecular Devices). Pipette solution contained 140 mM KCl, 10 mM HEPES, 5 mM ATP, with varying concentrations of IP_3, BAPTA, and free Ca^{2+}. Free [Ca^{2+}] was calculated using Max Chelator freeware and verified fluorometrically. Traces were consecutive 3-s sweeps recorded at −100 mV, sampled at 20 kHz, and filtered at 5 kHz. A minimum of 15 s of recordings were considered for data analyses. The data are representative of between three and five experiments for each condition presented. Pipette resistances were typically 20 MΩ and seal resistances were >5 GΩ (51).

Data Analysis. Single-channel openings were detected by half-threshold crossing criteria using the event detection protocol in Clampfit 9. We assumed that the number of channels in any particular nuclear patch is represented by the maximum number of discrete stacked events observed during the experiment. Even at low P_o, stacking events were evident. Only patches with one apparent channel were considered for analyses. Probability of opening (P_o), unitary current (i_k), open and closed times, and burst analyses were calculated using Clampfit 9 and Origin 6 software (OriginLab). All-points current amplitude histograms were generated from the current records and fitted with a normal Gaussian probability distribution function. The coefficient of determination (R^2) for every fit was >0.95. The P_o was calculated using the multimodal distribution for the open and closed current levels. The threshold for an open event was set at 50% of the maximum open current and events shorter than 0.1 ms were ignored. A "burst" was defined as a period of channel opening following a period of no channel activity, which was >5 times the mean closed time (0.2 ms) within a burst. Ca^{2+} dependency curves were fitted separately for activation and inhibition with the logistic equation:

$$Y = [(A1 - A2)/(1 + (X/X_0)p)] + A2,$$

where $A1$ and $A2$ are asymptotes, X is the concentration of Ca^{2+}, X_0 is the half-maximal concentration, and p is the slope related to the Hill coefficient. Equation parameters were estimated using a nonlinear, least-squares algorithm.

Statistical Analysis. All of the statistical tests were conducted in GraphPad Prism 9 and data are presented as the mean ± SD. Statistical significance was determined using one-way ANOVA with Tukey's test or the Mann-Whitney *U* test as indicated in the figure legends.

Data, Materials, and Software Availability. All of the study data are included in the article and/or *SI Appendix*.

ACKNOWLEDGMENTS. The authors wish to thank Dr. Kamil J. Alzayady, Ms. Taylor R. Knebel for generating stable cell lines, and all of the members of the Yule lab, especially Ms. Kai-Ting Huang and Ms. Amanda M. Wahl for their valuable suggestions. The authors wish to thank Dr. Ian Parker and Dr. Jeffrey Lock (both University of California, Irvine) for assistance and advice with FLIKA. This work was supported by National Institutes of Health grant NIH/DE019245, to D.I.Y.; NIH/R01GM132611, to S.K.J.; NIH/R01GM072804 and Welch Foundation research grant AU-2014-20220331, to I.I.S.; and American Heart Association grant 18CDA34110086, to M.R.B.

Author affiliations: [a]Department of Pharmacology and Physiology, University of Rochester, Rochester, NY 14642; [b]Department of Biochemistry and Molecular Biology, Structural Biology Imaging Center, McGovern Medical School, The University of Texas Health Science Center at Houston, Houston, TX 77030; and [c]Department of Pathology, Anatomy, and Cell Biology, Thomas Jefferson University, Philadelphia, PA 19107

1. M. J. Berridge, P. Lipp, M. D. Bootman, The versatility and universality of calcium signalling. *Nat. Rev. Mol. Cell Biol.* **1**, 11–21 (2000).
2. M. J. Berridge, P. Lipp, M. D. Bootman, Signal transduction. The calcium entry pas de deux. *Science* **287**, 1604–1605 (2000).
3. O. Blondel, J. Takeda, H. Janssen, S. Seino, G. I. Bell, Sequence and functional characterization of a third inositol trisphosphate receptor subtype, IP3R-3, expressed in pancreatic islets, kidney, gastrointestinal tract, and other tissues. *J. Biol. Chem.* **268**, 11356–11363 (1993).
4. T. Furuichi *et al.*, Primary structure and functional expression of the inositol 1,4,5-trisphosphate-binding protein P400. *Nature* **342**, 32–38 (1989).
5. A. R. Maranto, Primary structure, ligand binding, and localization of the human type 3 inositol 1,4,5-trisphosphate receptor expressed in intestinal epithelium. *J. Biol. Chem.* **269**, 1222–1230 (1994).
6. G. A. Mignery, T. C. Südhof, K. Takei, P. De Camilli, Putative receptor for inositol 1,4,5-trisphosphate similar to ryanodine receptor. *Nature* **342**, 192–195 (1989).
7. T. C. Südhof, C. L. Newton, B. T. Archer III, Y. A. Ushkaryov, G. A. Mignery, Structure of a novel InsP3 receptor. *EMBO J.* **10**, 3199–3206 (1991).
8. M. Iino, Biphasic Ca2+ dependence of inositol 1,4,5-trisphosphate-induced Ca release in smooth muscle cells of the guinea pig taenia caeci. *J. Gen. Physiol.* **95**, 1103–1122 (1990).
9. M. J. Berridge, The inositol trisphosphate/calcium signaling pathway in health and disease. *Physiol. Rev.* **96**, 1261–1296 (2016).
10. F. Yoshikawa *et al.*, Mutational analysis of the ligand binding site of the inositol 1,4,5-trisphosphate receptor. *J. Biol. Chem.* **271**, 18277–18284 (1996).
11. C. C. Lin, K. Baek, Z. Lu, Apo and $InsP_3$-bound crystal structures of the ligand-binding domain of an $InsP_3$ receptor. *Nat. Struct. Mol. Biol.* **18**, 1172–1174 (2011).
12. M. D. Seo *et al.*, Structural and functional conservation of key domains in InsP3 and ryanodine receptors. *Nature* **483**, 108–112 (2012).
13. G. Fan *et al.*, Gating machinery of InsP3R channels revealed by electron cryomicroscopy. *Nature* **527**, 336–341 (2015).
14. G. Fan *et al.*, Cryo-EM reveals ligand induced allostery underlying $InsP_3R$ channel gating. *Cell Res.* **28**, 1158–1170 (2018).
15. N. Paknejad, R. K. Hite, Structural basis for the regulation of inositol trisphosphate receptors by Ca^{2+} and IP_3. *Nat. Struct. Mol. Biol.* **25**, 660–668 (2018).
16. C. M. Azumaya, E. A. Linton, C. J. Risener, T. Nakagawa, E. Karakas, Cryo-EM structure of human type-3 inositol triphosphate receptor reveals the presence of a self-binding peptide that acts as an antagonist. *J. Biol. Chem.* **295**, 1743–1753 (2020).
17. H. Ando, M. Hirose, K. Mikoshiba, Aberrant IP_3 receptor activities revealed by comprehensive analysis of pathological mutations causing spinocerebellar ataxia 29. *Proc. Natl. Acad. Sci. U.S.A.* **115**, 12259–12264 (2018).
18. L. E. Terry, K. J. Alzayady, A. M. Wahl, S. Malik, D. I. Yule, Disease-associated mutations in inositol 1,4,5-trisphosphate receptor subunits impair channel function. *J. Biol. Chem.* **295**, 18160–18178 (2020).
19. K. J. Alzayady *et al.*, Defining the stoichiometry of inositol 1,4,5-trisphosphate binding required to initiate Ca2+ release. *Sci. Signal.* **9**, ra35 (2016).
20. I. Bezprozvanny, J. Watras, B. E. Ehrlich, Bell-shaped calcium-response curves of Ins(1,4,5)P3- and calcium-gated channels from endoplasmic reticulum of cerebellum. *Nature* **351**, 751–754 (1991).
21. J. K. Foskett, C. White, K. H. Cheung, D. O. Mak, Inositol trisphosphate receptor Ca2+ release channels. *Physiol. Rev.* **87**, 593–658 (2007).
22. E. A. Finch, T. J. Turner, S. M. Goldin, Calcium as a coagonist of inositol 1,4,5-trisphosphate-induced calcium release. *Science* **252**, 443–446 (1991).
23. E. J. Kaftan, B. E. Ehrlich, J. Watras, Inositol 1,4,5-trisphosphate (InsP3) and calcium interact to increase the dynamic range of InsP3 receptor-dependent calcium signaling. *J. Gen. Physiol.* **110**, 529–538 (1997).
24. D. O. Mak, S. McBride, J. K. Foskett, Inositol 1,4,5-trisphosphate [correction of tris-phosphate] activation of inositol trisphosphate [correction of tris-phosphate] receptor Ca2+ channel by ligand tuning of Ca2+ inhibition. *Proc. Natl. Acad. Sci. U.S.A.* **95**, 15821–15825 (1998).
25. D. O. Mak, S. McBride, J. K. Foskett, Regulation by Ca2+ and inositol 1,4,5-trisphosphate (InsP3) of single recombinant type 3 InsP3 receptor channels. Ca2+ activation uniquely distinguishes types 1 and 3 insp3 receptors. *J. Gen. Physiol.* **117**, 435–446 (2001).
26. I. C. Marshall, C. W. Taylor, Two calcium-binding sites mediate the interconversion of liver inositol 1,4,5-trisphosphate receptors between three conformational states. *Biochem. J.* **301**, 591–598 (1994).
27. C. W. Taylor, S. C. Tovey, IP(3) receptors: Toward understanding their activation. *Cold Spring Harb. Perspect. Biol.* **2**, a004010 (2010).
28. J. S. Marchant, C. W. Taylor, Cooperative activation of IP3 receptors by sequential binding of IP3 and Ca2+ safeguards against spontaneous activity. *Curr. Biol.* **7**, 510–518 (1997).
29. H. Vais, J. K. Foskett, G. Ullah, J. E. Pearson, D. O. Mak, Permeant calcium ion feed-through regulation of single inositol 1,4,5-trisphosphate receptor channel gating. *J. Gen. Physiol.* **140**, 697–716 (2012).
30. C. E. Adkins, C. W. Taylor, Lateral inhibition of inositol 1,4,5-trisphosphate receptors by cytosolic Ca(2+). *Curr. Biol.* **9**, 1115–1118 (1999).
31. J. T. Lock, K. J. Alzayady, D. I. Yule, I. Parker, All three IP_3 receptor isoforms generate Ca^{2+} puffs that display similar characteristics. *Sci. Signal.* **11**, eaau0344 (2018).
32. S. Mataragka, C. W. Taylor, All three IP_3 receptor subtypes generate Ca^{2+} puffs, the universal building blocks of IP_3-evoked Ca^{2+} signals. *J. Cell Sci.* **131**, jcs220848 (2018).
33. I. F. Smith, S. M. Wiltgen, J. Shuai, I. Parker, Ca(2+) puffs originate from preestablished stable clusters of inositol trisphosphate receptors. *Sci. Signal.* **2**, ra77 (2009).
34. D. L. Prole, C. W. Taylor, Structure and function of IP_3 receptors. *Cold Spring Harb. Perspect. Biol.* **11**, a035063 (2019).
35. I. Sienaert *et al.*, Characterization of a cytosolic and a luminal Ca2+ binding site in the type I inositol 1,4,5-trisphosphate receptor. *J. Biol. Chem.* **271**, 27005–27012 (1996).
36. I. Sienaert *et al.*, Molecular and functional evidence for multiple Ca2+-binding domains in the type 1 inositol 1,4,5-trisphosphate receptor. *J. Biol. Chem.* **272**, 25899–25906 (1997).
37. S. K. Joseph, S. Brownell, M. T. Khan, Calcium regulation of inositol 1,4,5-trisphosphate receptors. *Cell Calcium* **38**, 539–546 (2005).
38. H. Tu *et al.*, Functional and biochemical analysis of the type 1 inositol (1,4,5)-trisphosphate receptor calcium sensor. *Biophys. J.* **85**, 290–299 (2003).
39. T. Miyakawa *et al.*, Ca(2+)-sensor region of IP(3) receptor controls intracellular Ca(2+) signaling. *EMBO J.* **20**, 1674–1680 (2001).
40. A. des Georges *et al.*, Structural basis for gating and activation of RyR1. *Cell* **167**, 145–157.e17 (2016).
41. L. Xu *et al.*, Ca^{2+}-mediated activation of the skeletal-muscle ryanodine receptor ion channel. *J. Biol. Chem.* **293**, 19501–19509 (2018).
42. W. Guo *et al.*, The EF-hand Ca2+ binding domain is not required for cytosolic Ca2+ activation of the cardiac ryanodine receptor. *J. Biol. Chem.* **291**, 2150–2160 (2016).
43. M. R. Baker, G. Fan, I. I. Serysheva, Structure of IP_3R channel: High-resolution insights from cryo-EM. *Curr. Opin. Struct. Biol.* **46**, 38–47 (2017).
44. E. A. Schmitz, H. Takahashi, E. Karakas, Structural basis for activation and gating of IP_3 receptors. *Nat. Commun.* **13**, 1408 (2022).

45. G. Fan *et al.*, Structural dynamics underlying gating and regulation in IP$_3$R channel. bioRxiv (2022) https://www.biorxiv.org/content/10.1101/2022.05.27.493711v1. Accessed 28 June 2022.
46. K. Hamada, H. Miyatake, A. Terauchi, K. Mikoshiba, IP$_3$-mediated gating mechanism of the IP$_3$ receptor revealed by mutagenesis and X-ray crystallography. *Proc. Natl. Acad. Sci. U.S.A.* **114**, 4661–4666 (2017).
47. S. J. Ludtke *et al.*, Flexible architecture of IP3R1 by cryo-EM. *Structure* **19**, 1192–1199 (2011).
48. J. T. Lock, I. Parker, IP$_3$ mediated global Ca^{2+} signals arise through two temporally and spatially distinct modes of Ca^{2+} release. *eLife* **9**, e55008 (2020).
49. I. F. Smith, I. Parker, Imaging the quantal substructure of single IP3R channel activity during Ca2+ puffs in intact mammalian cells. *Proc. Natl. Acad. Sci. U.S.A.* **106**, 6404–6409 (2009).
50. I. F. Smith, S. M. Wiltgen, I. Parker, Localization of puff sites adjacent to the plasma membrane: Functional and spatial characterization of Ca2+ signaling in SH-SY5Y cells utilizing membrane-permeant caged IP3. *Cell Calcium* **45**, 65–76 (2009).
51. L. E. Wagner II, D. I. Yule, Differential regulation of the InsP$_3$ receptor type-1 and -2 single channel properties by InsP$_3$, Ca^{2+} and ATP. *J. Physiol.* **590**, 3245–3259 (2012).
52. M. J. Betzenhauser *et al.*, ATP modulation of Ca2+ release by type-2 and type-3 inositol (1, 4, 5)-triphosphate receptors. Differing ATP sensitivities and molecular determinants of action. *J. Biol. Chem.* **283**, 21579–21587 (2008).
53. M. J. Betzenhauser, L. E. Wagner II, H. S. Park, D. I. Yule, ATP regulation of type-1 inositol 1,4,5-trisphosphate receptor activity does not require walker A-type ATP-binding motifs. *J. Biol. Chem.* **284**, 16156–16163 (2009).
54. D. O. Mak, S. McBride, J. K. Foskett, ATP regulation of type 1 inositol 1,4,5-trisphosphate receptor channel gating by allosteric tuning of Ca(2+) activation. *J. Biol. Chem.* **274**, 22231–22237 (1999).
55. T. Jean, C. B. Klee, Calcium modulation of inositol 1,4,5-trisphosphate-induced calcium release from neuroblastoma x glioma hybrid (NG108-15) microsomes. *J. Biol. Chem.* **261**, 16414–16420 (1986).
56. E. Suematsu, M. Hirata, T. Hashimoto, H. Kuriyama, Inositol 1,4,5-trisphosphate releases Ca2+ from intracellular store sites in skinned single cells of porcine coronary artery. *Biochem. Biophys. Res. Commun.* **120**, 481–485 (1984).
57. I. Parker, I. Ivorra, Inhibition by Ca2+ of inositol trisphosphate-mediated Ca2+ liberation: A possible mechanism for oscillatory release of Ca2+. *Proc. Natl. Acad. Sci. U.S.A.* **87**, 260–264 (1990).
58. I. C. Marshall, C. W. Taylor, Biphasic effects of cytosolic Ca2+ on Ins(1,4,5)P3-stimulated Ca2+ mobilization in hepatocytes. *J. Biol. Chem.* **268**, 13214–13220 (1993).
59. L. Stehno-Bittel, A. Lückhoff, D. E. Clapham, Calcium release from the nucleus by InsP3 receptor channels. *Neuron* **14**, 163–167 (1995).
60. D. Boehning, S. K. Joseph, D. O. Mak, J. K. Foskett, Single-channel recordings of recombinant inositol trisphosphate receptors in mammalian nuclear envelope. *Biophys. J.* **81**, 117–124 (2001).
61. G. A. Mignery, P. A. Johnston, T. C. Südhof, Mechanism of Ca2+ inhibition of inositol 1,4,5-trisphosphate (InsP3) binding to the cerebellar InsP3 receptor. *J. Biol. Chem.* **267**, 7450–7455 (1992).
62. K. J. Alzayady *et al.*, Tracing the evolutionary history of inositol, 1, 4, 5-trisphosphate receptor: Insights from analyses of Capsaspora owczarzaki Ca2+ release channel orthologs. *Mol. Biol. Evol.* **32**, 2236–2253 (2015).
63. R. Joshi, K. Venkatesh, R. Srinivas, S. Nair, G. Hasan, Genetic dissection of itpr gene function reveals a vital requirement in aminergic cells of Drosophila larvae. *Genetics* **166**, 225–236 (2004).
64. S. Srikanth *et al.*, Functional properties of the Drosophila melanogaster inositol 1,4,5-trisphosphate receptor mutants. *Biophys. J.* **86**, 3634–3646 (2004).
65. M. D. Bootman, M. J. Berridge, P. Lipp, Cooking with calcium: The recipes for composing global signals from elementary events. *Cell* **91**, 367–373 (1997).
66. N. B. Thillaiappan, H. A. Smith, P. Atakpa-Adaji, C. W. Taylor, KRAP tethers IP$_3$ receptors to actin and licenses them to evoke cytosolic Ca^{2+} signals. *Nat. Commun.* **12**, 4514 (2021).
67. V. Arige *et al.*, CREB regulates the expression of type 1 inositol 1,4,5-trisphosphate receptors. *J. Cell Sci.* **134**, jcs258875 (2021).
68. N. B. Thillaiappan, A. P. Chavda, S. C. Tovey, D. L. Prole, C. W. Taylor, Ca^{2+} signals initiate at immobile IP$_3$ receptors adjacent to ER-plasma membrane junctions. *Nat. Commun.* **8**, 1505 (2017).
69. M. Iwai, T. Michikawa, I. Bosanac, M. Ikura, K. Mikoshiba, Molecular basis of the isoform-specific ligand-binding affinity of inositol 1,4,5-trisphosphate receptors. *J. Biol. Chem.* **282**, 12755–12764 (2007).
70. H. Sugawara, M. Kurosaki, M. Takata, T. Kurosaki, Genetic evidence for involvement of type 1, type 2 and type 3 inositol 1,4,5-trisphosphate receptors in signal transduction through the B-cell antigen receptor. *EMBO J.* **16**, 3078–3088 (1997).
71. K. J. Alzayady, R. Chandrasekhar, D. I. Yule, Fragmented inositol 1,4,5-trisphosphate receptors retain tetrameric architecture and form functional Ca2+ release channels. *J. Biol. Chem.* **288**, 11122–11134 (2013).
72. K. L. Ellefsen, B. Settle, I. Parker, I. F. Smith, An algorithm for automated detection, localization and measurement of local calcium signals from camera-based imaging. *Cell Calcium* **56**, 147–156 (2014).
73. V. Arige, S. M. Emrich, R. E. Yoast, M. Trebak, D. I. Yule, A protocol for detecting elemental calcium signals (Ca^{2+} puffs) in mammalian cells using total internal reflection fluorescence microscopy. *STAR Protoc* **2**, 100618 (2021).